Photon beam polarization by analysis of data from the Hall D Triplet Polarimeter

M. Dugger, N. Sparks, B.G. Ritchie
Arizona State University, Tempe, AZ 85287-1504

1 Introduction

The triplet polarimeter (TPOL) determines the degree of polarization of the incident photon beam by using the process of triplet photoproduction. In the triplet photoproduction process, the polarized photon beam interacts with the electric field of an atomic electron (rather than the field of the atomic nucleus) within the material of a production target, and produces a high energy electron-positron pair through the pair production process. The atomic electron on which the pair production took place then recoils with sufficient momentum to leave the atom. Any momentum of the electron-positron pair transverse to the incoming photon beam must be compensated by the momentum of the recoil electron. The recoil electron momentum is much smaller than that of either of the pair-produced leptons, so that the recoil electron can attain a large polar scattering angle relative to the axis determined by the incoming photon beam. The azimuthal angular distribution of the recoil electron yields information on the beam polarization.

The cross section for triplet photoproduction can be written as $\sigma_t = \sigma_0 \left[1 + P\Sigma \cos(2\phi)\right]$ for a polarized photon beam, where σ_0 is the unpolarized cross section, P is the photon beam polarization, Σ is the beam asymmetry, and ϕ is the azimuthal angle of the recoil electron. For GlueX, the photoproduced pair is detected in the pair spectrometer downstream of the triplet polarimeter. The process is purely governed by QED, and thus a QED calculation of the beam asymmetry can determine the analyzing power of the reaction.

To determine the photon beam polarization, the azimuthal distribution of the recoil electrons is recorded and fit to the function $A\left[1 + B\cos(2\phi)\right]$, where the variables A and B are parameters of the fit. Once B has been extracted from the data, the degree of photon beam polarization is given by $P = B/\Sigma$.

2 Event generator

The event generator used in simulating the pair production process includes all 8 tree-level QED diagrams (see Fig. 1), with corrections due to the incoherent scattering function (also referred to as the screening correction) included.

2.1 $\gamma\gamma$-like diagrams

The diagrams (a) and (b) in Fig. 1 are referred to here as "$\gamma\gamma$-like." These two diagrams look like the reaction $\gamma\gamma \rightarrow e^+e^-$, where one of the γ legs is connected to an electron at position 0 that scatters to position 4.

The matrix elements for the $\gamma\gamma$-like diagrams are given by

$$-iM_a \equiv (ig_e)^3 \left(\tfrac{-i}{q_2^2}\right) \quad \left[\overline{u}_2 \gamma^\mu i \left(\frac{\not{p}_1 - \not{p}_3 + m}{(p_1 - p_3)^2 - m^2}\right) \not{\epsilon}_1 v_3\right] \left[\overline{u}_4 \gamma_\mu u_0\right], \tag{1}$$

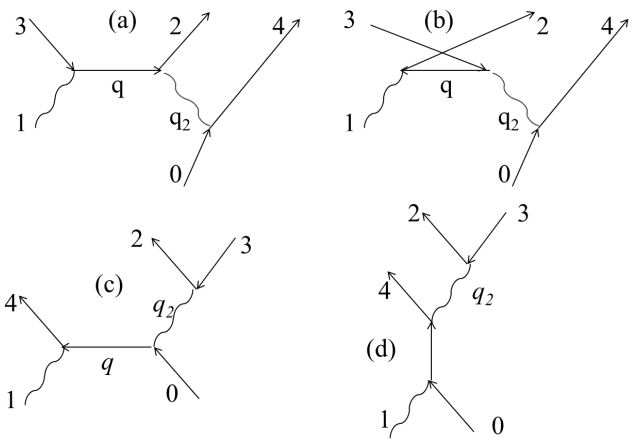

Figure 1: This figure illustrates one-half of the Feynman diagrams involved in the triplet photoproduction process; the remaining half is obtained by crossing the electron at 2 with the electron at 4. Diagrams (a) and (b) are referred to as "$\gamma\gamma$-like", while diagrams (c) and (d) are said to be "Compton-like." For the figures, line 0 indicates the target electron, line 1 indicates the incident photon, line 2 (3) indicates the pair-produced electron (positron), and line 4 indicates the recoil atomic electron.

$$-iM_b \equiv (ig_e)^3 \left(\tfrac{-i}{q_2^2}\right) \quad \left[\overline{u}_2 \not{\epsilon}_1 i \left(\frac{\not{p}_2 - \not{p}_1 + m}{(p_2 - p_1)^2 - m^2}\right) \gamma^\mu v_3\right] \left[\overline{u}_4 \gamma_\mu u_0\right], \tag{2}$$

where γ_μ represents the Dirac matrices, m the electron mass, q_2^2 the mass of the virtual photon, p ($\not{p}$) the four-momentum (product of four-momentum with the Dirac matrices), u and v represent spinors, $\overline{u}$ is an adjoint spinor, $\not{\epsilon}_1$ is the product of incident photon polarization and Dirac matrices, and the coupling constant g_e is equal to $\sqrt{4\pi\alpha}$, with α being the fine structure constant. The subscripts 0, 1, 2, 3, and 4 represent the target electron, incident photon, outgoing electron, outgoing positron, and recoil electron, respectively.

The matrix elements for the crossed $\gamma\gamma$-like diagrams (which are not shown in Fig. 1) are found by switching legs 2 and 4 of diagrams (a) and (b) in Fig. 1. Those matrix elements are written as

$$-iM_{a2} \equiv (ig_e)^3 \left(\tfrac{i}{q_2^2}\right) \quad \left[\overline{u}_4 \gamma^\mu i \left(\frac{\not{p}_1 - \not{p}_3 + m}{(p_1 - p_3)^2 - m^2}\right) \not{\epsilon}_1 v_3\right] \left[\overline{u}_2 \gamma_\mu u_0\right], \tag{3}$$

$$-iM_{b2} \equiv (ig_e)^3 \left(\tfrac{i}{q_2^2}\right) \quad \left[\overline{u}_4 \not{\epsilon}_1 i \left(\frac{\not{p}_4 - \not{p}_1 + m}{(p_4 - p_1)^2 - m^2}\right) \gamma^\mu v_3\right] \left[\overline{u}_2 \gamma_\mu u_0\right]. \tag{4}$$

2.2 Compton-like diagrams

Diagrams (c) and (d) in Fig. 1 are referred to here as "Compton-like." These two diagrams look like the reaction $\gamma p \to \gamma p$, where the scattered γ leg is connected to an electron-positron creation vertex.

The matrix elements for the Compton-like diagrams are given by

$$-iM_c \equiv (ig_e)^3 \left(\tfrac{-i}{q_2^2}\right) \quad \left[\overline{u}_4 \not{\epsilon}_1 i \frac{\not{p}_4 - \not{p}_1 + m}{(p_4 - p_1)^2 - m^2} \gamma^\mu u_0\right] [\overline{u}_2 \gamma_\mu v_3], \tag{5}$$

$$-iM_d \equiv (ig_e)^3 \left(\tfrac{-i}{q_2^2}\right) \quad \left[\overline{u}_4 \gamma^\mu i \frac{\not{p}_1 + \not{p}_0 + m}{(p_1 + p_0)^2 - m^2} \not{\epsilon}_1 u_0\right] [\overline{u}_2 \gamma_\mu v_3]. \tag{6}$$

Switching legs 2 and 4 in diagrams (c) and (d) in Fig. 1 gives us the crossed Compton-like diagrams:

$$-iM_{c2} \equiv (ig_e)^3 \left(\tfrac{i}{q_2^2}\right) \quad \left[\overline{u}_2 \not{\epsilon}_1 i \frac{\not{p}_2 - \not{p}_1 + m}{(p_2 - p_1)^2 - m^2} \gamma^\mu u_0\right] [\overline{u}_4 \gamma_\mu v_3], \tag{7}$$

$$-iM_{d2} \equiv (ig_e)^3 \left(\tfrac{i}{q_2^2}\right) \quad \left[\overline{u}_2 \gamma^\mu i \frac{\not{p}_1 + \not{p}_0 + m}{(p_1 + p_0)^2 - m^2} \not{\epsilon}_1 u_0\right] [\overline{u}_4 \gamma_\mu v_3]. \tag{8}$$

2.3 Total matrix element for triplet photoproduction

By including the matrix elements shown in Fig. 1 and those given by crossing lines 2 and 4, the full matrix element for the triplet photoproduction is calculable. The total matrix element M_{tot} is simply the sum of the eight matrix elements provided in Equations 1-8 above:

$$M_{\text{tot}} = M_a + M_b + M_c + M_d + M_{a2} + M_{b2} + M_{c2} + M_{d2}. \tag{9}$$

2.4 Screening correction

The correction due to the screening function ($S(q)$) for triplet production on hydrogen is related to the atomic form factor ($F(q)$) [1] such that

$$S(q) = 1 - F^2(q), \tag{10}$$

where $F(q) = (1 + a^2q^2/4)^{-2}$, q is the momentum transfer, and a is the Bohr radius.

For the triplet process described in this document we use the beryllium screening function found in [4].

2.5 Cross section

Using this event generator, the calculation of the cross section proceeds in a straightforward fashion. The phase space for the reaction is randomly generated event-by-event using an algorithm provided by Richard Jones. For each event, the matrix element $|M_{\text{tot}}|^2$ is constructed from Equation 9 and then averaged over initial spins and summed over final spins to obtain $\langle |M_{\text{tot}}|^2 \rangle$. For the case where the incident photon is polarized, the spin state of the photon is locked in value when averaging over the initial spin states. A value for the cross section is obtained using

$$\frac{d\sigma}{d\Omega} = \frac{(2\pi)^2}{4km} \left\langle |M_{\text{tot}}|^2 \right\rangle \rho_f S(q), \tag{11}$$

where k is the incident photon energy and ρ_f represents the final-state phase space. Each event is then assigned a weight equal to the calculated cross section.

The results from this event generator may be compared to the National Institute of Standards and Technology (NIST) cross sections for beryllium [2]. Such a comparison is presented in Fig. 2. In that figure, the solid black line represents the value of the total cross section given by NIST, and the results from the event generator are shown as solid squares; the results without the incoherent scattering function are shown as blue, while red squares denote the results when incoherent scattering function has been included. As can been seen from the figure, the agreement between the event generator and NIST is excellent when the incoherent scattering function is included.

The agreement seen in Fig. 2 demonstrates that the process has been adequately described by Equations 1-8 above.

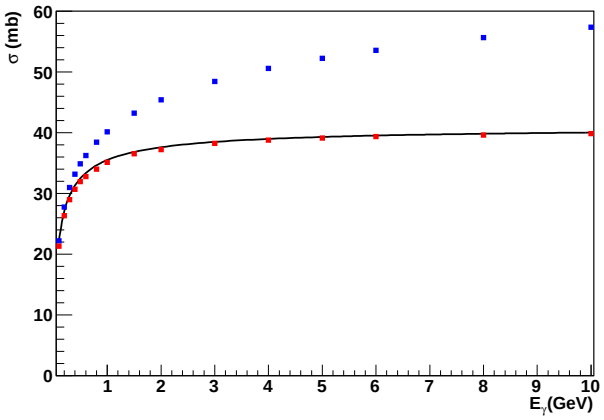

Figure 2: The total cross section for triplet photoproduction for beryllium as a function of incident photon energy. The red (blue) squares represent generator results with (without) screening. The solid black line represents the NIST values.

3 Triplet polarimeter detector and electronics

3.1 Silicon strip detector

The triplet polarimeter (TPOL) consists of a vacuum chamber containing a movable tray holding a selection of production target foils, a silicon strip detector for detecting the recoil electron, and cabling connecting the detector and drive motors to associated electronics through vacuum feedthroughs. The vacuum chamber is physically located in the Hall D collimator cave just upstream of the pair spectrometer. The various components of the TPOL are described in brief detail here.

The timing information, energy deposition, and azimuthal angle of the recoil electron, coming from the atomic electron in the triplet process, are measured by a double-sided silicon strip detector (SSD). For this system, a SSD manufactured by Micron Semiconductor (model S3) was selected. The S3 has 32 azimuthal sectors on the ohmic side and 24 concentric rings on the junction side. The S3 has an outer active diameter of 70 mm and an inner active diameter of 22 mm. The thickness of the silicon is 1034 microns. As manufactured, the semiconductor material is fully depleted using a bias potential of 165 V, with a manufacturer's suggested potential of 200 V.

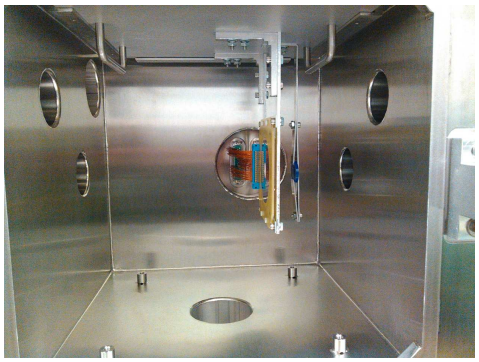

Figure 3: Interior view of the vacuum chamber with detachable plate, detector, source stand and source (blue disk). Note: The converter positioning system was removed when this photograph was taken.

An inside view of the chamber, with converter positioning system removed, can be seen in Fig. 3. The SSD is mounted in a yellow printed circuit board that is attached to two one-eighth-inch-thick aluminum crossbars at the top and bottom of the board. In turn, those crossbars are attached to

vertical legs that are affixed to L-shaped supports; the L-shaped supports are then mounted on the removable plate.

3.2 Preamplifiers

A photon passing through the depletion region of a semiconductor loses energy through the creation of electron-hole pairs in the material. An electron-hole pair is created for each 3.6 eV of energy deposited. The electrons are collected on the positive side of the potential (sector side of the detector), while the holes are swept towards the ring side (ground).

A circuit diagram for a simplified and generic charge-sensitive preamplifier is shown in Fig. 4. The actual preamplifiers used in this instrument were custom built by David Swan, and are more complicated than the design shown in Fig. 4. However, the Swan preamplifiers nonetheless still contain all the elements shown, and the figure can be used to discuss the operation of the custom electronics utilized here.

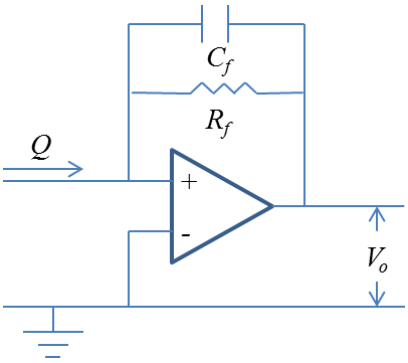

Figure 4: Circuit diagram of a generic charge-sensitive preamplifier.

Of particular importance in the operation of the TPOL electronics are the feedback capacitance (C_f) and resistance (R_f). For our application, $C_f = 0.2$ pF and $R_f = 30$ MΩ were chosen. The fall time τ_F for the preamplifier is simply $R_f C_f$, and, thus, in our case $\tau_F = 6$ μs. The rise time for the signal is determined by the charge collection time of the detector and by the response time of the preamplifier. The optimal sensitivity (S_o) of the preamplifier is determined by the feedback capacitance such that $S_o = 1/C_f$, which leads to $S_o \approx 250$ mV/MeV.

Electronic filters/amplifiers were added to the output of the charge-sensitive preamplifiers in order to reduce unwanted noise and to provide a small amount of signal shaping.

4 Simulation

The TPOL components and geometry were coded into a GEANT4 simulation of the triplet polarimeter. The event generator described above was used to model the triplet photoproduction within the production target material.

The production target (or converter) for the polarimeter is placed 33.7 mm upstream of the detector such that the photon beam strikes the converter material roughly in the center of the foil. For each generated triplet photoproduction event, the production vertex was distributed isotropically in the beamline direction (z) throughout the converter thickness, while the profile of the vertex distribution orthogonal to z used a realistic beam spot that was collimated within a diameter of 5 mm. For the simulation, the generator used a 76.2 μm thick beryllium converter, with incident photon energies ranging from 7 to 11 GeV.

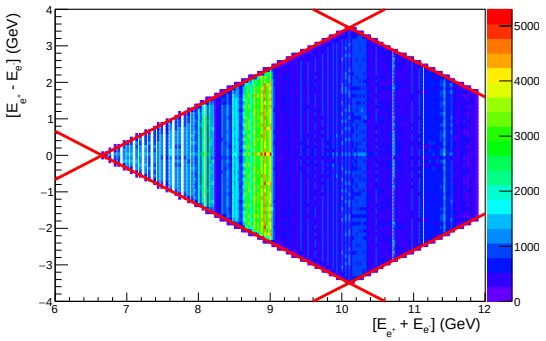

Figure 5: Plot of $\Delta(E_{\text{pair}})$ versus energy of pair for experimental PS data. The region between the red lines represents the fiducial region.

4.1 Triplet asymmetry

The generated events are passed through the GEANT4 detector simulation. In order to model the energy resolution of the detector and associated electronics, the energy deposition for each sector is randomly reassigned by way of a normal distribution centered at the observed energy with a standard deviation of 30 keV (the choice of standard deviation is explained later in this document). Within any given simulated TPOL event, a TPOL hit is defined as a single sector having energy deposition greater than 160 keV. Once the number of TPOL hits has been established for a simulated event, only those events that have a single TPOL hit with that hit having an energy deposition greater than 230 keV are further processed. Additionally, events are required to have an associated pair energy that is compatible with the energy acceptance of the Pair Spectrometer (PS).

The energy difference of the pair is defined as $\Delta(E_{\rm pair}) \equiv E_{e^+} - E_{e^-}$, where E_{e^+} (E_{e^-}) is the energy of the produced positron (electron). For a pair to be considered valid, the following inequalities must hold: $|\Delta(E_{\rm pair})| < \Delta(E_{\rm max1})$ and $|\Delta(E_{\rm pair})| < \Delta(E_{\rm max2})$, where

$$\begin{aligned} \Delta(E_{\rm max1}) &\equiv +1.0(E_{e^+} + E_{e^-}) - 6.6 \text{ GeV} \\ \Delta(E_{\rm max2}) &\equiv -1.0(E_{e^+} + E_{e^-}) + 13.6 \text{ GeV}. \end{aligned}$$

A plot showing the events within the fiducial region can be found in figure 5.

To obtain the azimuthal yield distribution, the Monte Carlo events passing the above criteria have the sector hits binned in incident photon energy and azimuthal angle, with each event weighted by the cross section. For each photon energy bin, the azimuthal yield distribution is fit to the function $A_{t\delta}[1 + B_{t\delta}\cos(2\phi)]$, where $B_{t\delta}$ represents the beam asymmetry of both triplet events and $\delta-$ray contributions that arise from triplets passing through the converter material.

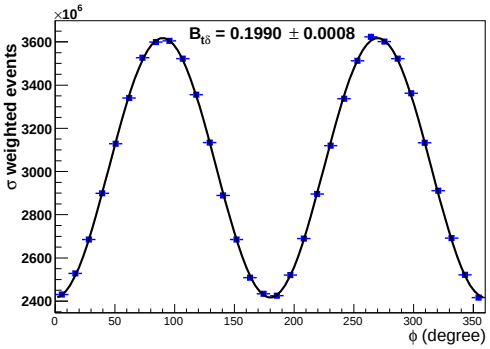

Figure 6: Analyzing power extraction. The blue points are cross section weighted Monte Carlo data for triplet events with incident photon beam energies between 8.5 and 8.6 GeV (including $\delta-$rays). The black line represents a fit of the data to $A_{t\delta}[1 + B_{t\delta}\cos(2\phi)]$, where $A_{t\delta}$ and $B_{t\delta}$ are parameters of the fit. For this energy, the value of $B_{t\delta}$ is shown on the plot and has a value of $B_{t\delta} = 0.1990(8)$.

For the determination of the analyzing power (Σ), the effect of $\delta-$rays coming from the leptons resulting from the pair production process must be included. We include the pair induced $\delta-$ray contribution to Σ by way of dilution. Essentially, if we were to include $\delta-$rays from the pair process, the equation for the yield (Y) would be given as

$$Y = A_{t\delta}[1 + B_{t\delta}\cos(2\phi)] + A_{p\delta},$$

where the yield from the pair produced $\delta-$rays is given as $A_{p\delta}$. This expression may be rewritten as

$$Y = A[1 + \Sigma\cos(2\phi)],$$

where

$$\begin{aligned} A &\equiv A_{t\delta} + A_{p\delta}, \\ \Sigma &= B_{t\delta}\frac{A_{t\delta}}{A}. \end{aligned} \tag{12}$$

From the above equation, the analyzing power is seen to be the $B_{t\delta}$ asymmetry diluted by a factor of $A_{t\delta}/A$. Therefore, a dilution factor can be defined as $d = A_{t\delta}/A$, leading to the result $\Sigma = B_{t\delta}d$.

The value of $A_{p\delta}$ is found by allowing only the created pairs from the generated triplet events to be processed through the detector simulation. The integrated detector response, weighted by the triplet cross section and passing all of the analysis cuts, is then scaled by the ratio $R_{pt} = \sigma_p/\sigma_t$, where σ_p (σ_t) is the pair (triplet) production cross section given by NIST. For beryllium, R_{pt} is found to vary quite slowly with energy, from $R_{pt} = 3.38$ at 8 GeV to $R_{pt} = 3.37$ at 10 GeV.

For the $B_{t\delta}$ asymmetry shown in Fig. 6, the dilution factor has a value of $d = 0.9575$, which leads to an analyzing power of $\Sigma = 0.1905(7)$.

4.2 Pair Spectrometer acceptance correction

The PS has, in addition to the energy dependent acceptance, an acceptance based on the height of the individual PS detector elements. The nominal distance from the converter foil to a PS detector element is 7.5 m and the height of the PS detectors is 3 cm.

We performed a simulation that included a realistic beam spot, the nominal distance the created pair travel before striking a PS detector and the PS detector height. When including these relevant PS geometric considerations, the asymmetry increased by a factor of 1.0026 for the case where the incident photon was parallel to the floor (PARA) and for the case where the incident photon was perpendicular to the laboratory floor (PERP), the asymmetry increased by a factor of 1.0057. These correction factors were then accounted for in the final determination of the beam polarization.

4.3 Beam offset study

The observed recoil electron asymmetry is altered if the detector and photon beam are not precisely coaxial. The effect of an offset in beam position, transverse to the detector center, has been explored by simulating the detector response for different values of beam offset using unpolarized generated events.

For the initial beam offset study we used an unpolarized beam spot uniform over a 5 mm disk. Twenty evenly spaced beam offsets ranging from 0.1 mm to 2.0 mm were analyzed. Fig. 7 shows a plot of cross-section-weighted events in blue for events generated with a 1-mm beam offset in the x-direction. Additionally, the figure shows a solid black line that represents a fit to the data, where the fit function is given by $A[1 + F_0 \cos(\phi)]$, with A and F_0 being fit parameters. As can be seen from the figure, the function appears to fit the result well, and in this case, produces a value of $F_0 = 0.089(1)$. In a similar manner, values of F_0 were determined for each of the generated beam offsets. The dependence of F_0 on the amount of generated beam offset is remarkably linear. A visual representation of the linearity between F_0 and the offset value can be found in Fig. 8.

Fortunately, the beam offset mainly causes the data to exhibit only zeroth- and first-order Fourier moments, and, due to orthogonality, the beam offset has only a small impact on the extraction of the second cosine moment, which is used to determine the beam asymmetry.

As will be discussed later in this document, the beam offset is typically rather small due to the care taken in aligning the TPOL with the beamline. For the first priority set from the Spring 2016 runs, the extracted value of F_0 is 0.011(1) and roughly corresponds to a beam offset of about 100 μm relative to the center line of the TPOL detector.

In order to more accurately mimic the actual incident photon, we used a realistic beam spot supplied by Richard Jones. The beam spot was collimated to have a diameter of 5.0 mm and was allowed to be displaced relative to the collimator center in steps of 0.1 mm from the nominal position

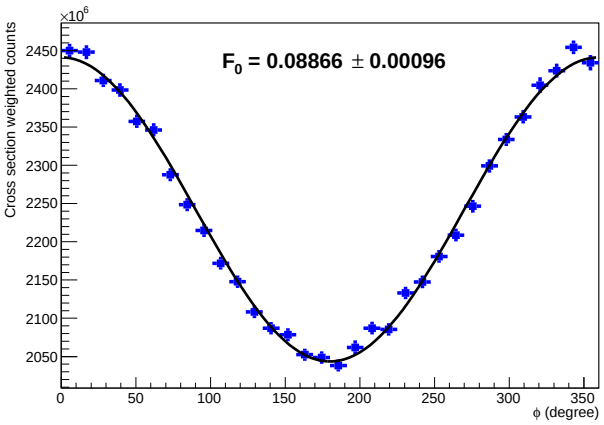

Figure 7: The blue points are unpolarized Monte Carlo data with the incident photon-beam offset from the detector center by 1.0 mm in the x-direction. The solid line is a fit of the data with the function $A[1 + F_0 \cos(\phi)]$, where A and F_0 are parameters of the fit. The value of F_0 is shown on the plot and has a value of 0.089(1).

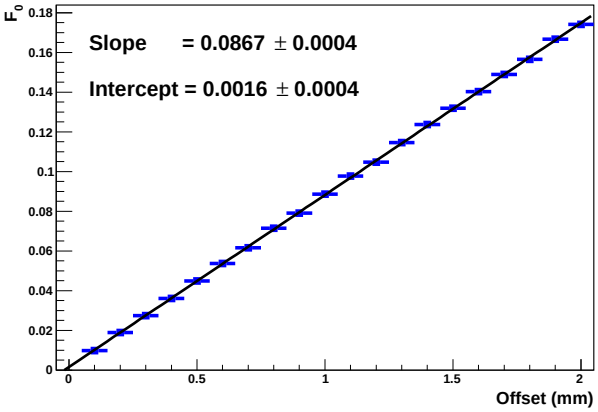

Figure 8: Plot of F_0 versus beam offset in mm. The blue points are from fit results, and the solid line is a first degree polynomial fit to the data, where the slope and intercept are displayed on the figure.

over a grid with eleven bins in the horizontal (x_B) and vertical (y_B) directions. In addition to the beam center displacement relative to the collimator center, the collimator was varied in vertical displacement relative to the TPOL center. The horizontal (vertical) coordinate of the collimator relative to the TPOL center is called x_0 (y_0). The values of vertical displacement studied were y_0 = 0.0, 0.1, 0.2, 0.3, 0.4, 0.5 mm. In all cases the horizontal displacement of the collimator relative to the TPOL center was fixed to x_0= 0.0.

The number of beam spot positions generated relative to the collimator center was 121 and the number of collimator positions relative to the TPOL center was 6. Thus, the total number of beam spot/collimator positions studied was 726. From the set of 726 combinations of beam spot and collimator positions, the value of F_0 was found. Since the value of F_0 determined from actual data was ≈0.01, we took as a conservative estimate of possible beam/collimator positions, those cases where $F_0 < 0.0225$. The requirement that $F_0 < 0.0225$ reduced the set of 726 combinations of beam spot and collimator positions to 30 cases that were further analyzed. From the 30 cases of beam/collimator positions compatible with the restriction that $F_0 < 0.0225$, the largest deviation from the ideal case (100% polarized beam with collimator and beam centered on TPOL) was found to be 0.71%.

5 Analysis of Spring 2016 data

As was discussed in Section 3.2, an electron-hole pair is created for each 3.6 eV of energy that was deposited in the silicon strip detector (SSD). The electronic signal from the SSD was then amplified, filtered, and passed to a flash ADC. The flash ADC used for the TPOL in the Spring 2016 running had 4096 channels distributed uniformly over a 2-volt range with a 250 MHz sampling rate.

For the first priority data set from Spring 2016, the ADC threshold for the amplified and filtered SSD signal was set to 133 ADC counts. The ADC crate information was read out whenever a signal above threshold was in coincidence with a GlueX or pair spectrometer (PS) trigger. PS-triggered events were skimmed from the full dataset for further analysis. The PS skim included relevant PS, TPOL, and tagger information, and all the variables required for further analysis were placed into a ROOT tree.

The SPICE-generated waveform simulation of the signals emerging from the TPOL electronics was created by using the LTspice IV program (electronic circuit simulator) [3], with a custom representation of the preamp/filter/amplifier electronics. The input signal for the LTspice program was a 10 μA pulse over a 5-ns duration (3.12 $\times 10^5$ electrons), corresponding to about 1.12 MeV of energy deposition when assuming an electron-hole pair for each 3.6 eV.

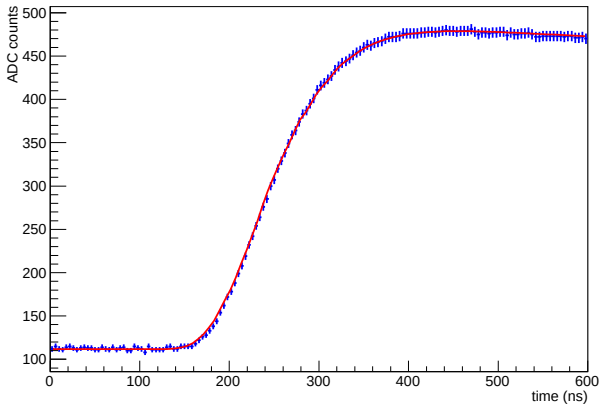

Figure 9: TPOL SSD signal ADC counts versus time for a typical event. The blue points are the data, while the red solid line represents the fit of the data to the SPICE waveform. (The error bars shown on the signal ADC counts are not meaningful and should be ignored.)

Within an event, every sector with a maximum ADC value greater than the readout threshold (133 ADC counts) was fit to the SPICE-generated waveform plus a constant (representing the baseline). The magnitude, time of the signal, and baseline constant were the only variables allowed to vary. A typical fit of the data to the SPICE waveform is shown in Fig. 9, where the data are shown as blue points and the resulting SPICE waveform fit is represented as a solid red line. As seen in the figure, the shape of the SPICE waveform represents the data well.

To calibrate the simulation of energy deposition in the device, the energy determined by the SPICE fit was taken as an initial estimate. The peak energy was then matched to the value given by the Monte Carlo using a single multiplicative constant for each sector. The initial energy given by the SPICE fit was generally very close to the final value, with the calibration constant for any given sector only differing from unity by about 10%.

For the time information in the simulation, the point along the fitted waveform halfway between the minimum and maximum signal voltage was taken to correspond to the time of the signal.

Figure 10 shows the timing of the TPOL events, where the blue region is where the TPOL in-time events are defined, and the red regions are the TPOL out-of-time events. For low energy recoil electrons that deposit all of their energy close to the upstream side of the SSD, the signal formation, consisting of the generated electrons and holes, is delayed when compared to the minimum ionizing case. This delay in the signal formation causes a tail in the timing distribution shown in the blue region of Fig. 10 that ranges from about 170 to 210 ns. The tagger time spectrum is shown in Fig. 11. For the tagger, the in-time events are defined as being within $\pm$ 2 ns and the out-of-time events are defined as being the two beam-buckets that have tagger time between -14 and -6 ns.

To determine the energy resolution of the triplet polarimeter, a plot of energy deposition from data was compared to energy deposition from Monte Carlo where the simulated results had differing resolutions applied. The manner in which the detector resolution was expressed in the simulation was by smearing the Monte Carlo energy deposition using a normal distribution. For each generated event, the value of energy deposition found from the simulated detector response was replaced by

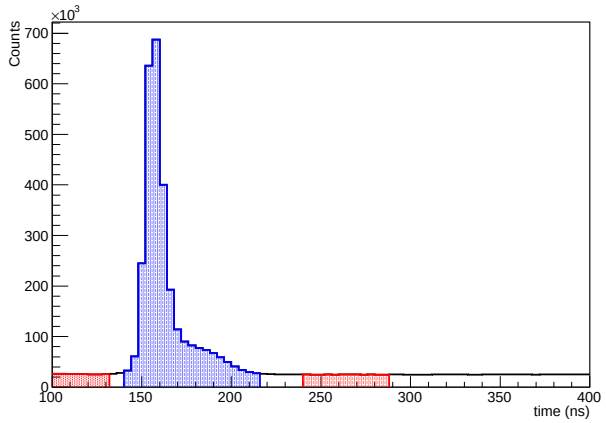

Figure 10: TPOL time relative to the PS trigger. The blue region represents events that are considered as being in time. The red regions are where out-of-time events are defined.

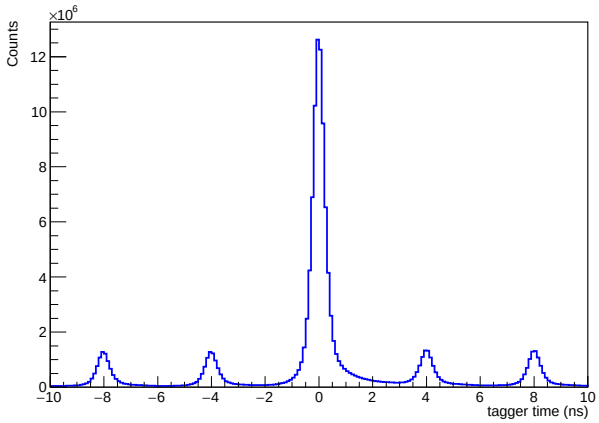

Figure 11: Tagger time relative to the PS trigger.

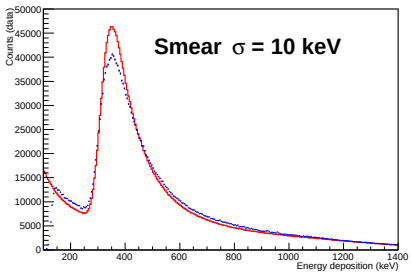

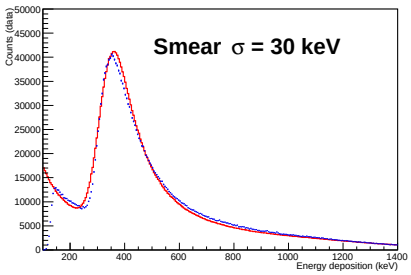

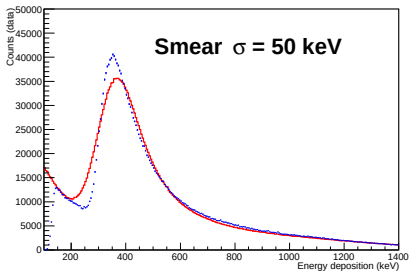

Figure 12: Energy deposition. Blue represents data. Red is Monte Carlo with standard deviation of smear parameter set to value shown on plots.

a random value arising from a normal distribution that had a center coinciding with the original energy deposition and a fixed standard deviation. The standard deviation of the normal distribution then corresponded to the detector/electronics resolution of the TPOL.

Several values of TPOL resolution were explored in the Monte Carlo study of energy deposition. Of the resolution values explored, some are shown in Fig. 12, with the standard deviation of the smeared energy shown on the plots. As can be seen in Fig. 13 and the middle panel of Fig. 12, smearing the energy deposition using a value for the standard deviation equal to 30 keV appeared to replicate the data fairly well. To try and determine how far off the data is from the simulation, a double Gaussian function was created that represents how to potentially shift the data to better align with the simulation results. The double Gaussian "shift function" is shown in Fig. 14 and gives the potential shift in energy deposition versus the value of energy deposition seen in the data. Using the double Gaussian given in Fig. 14, we produce the comparison of Monte Carlo to shifted real data seen in Fig. 15. As shown in Fig. 15 the comparison of the shifted data to the simulation results is very good. We take this to mean that the energy calibration can be off as much as 80 keV. The possible systematics associated with this uncertainty in the energy calibration and energy resolution will be discussed later in this document.

The actual TPOL events from the Spring 2016 first priority data set that passed the same cuts

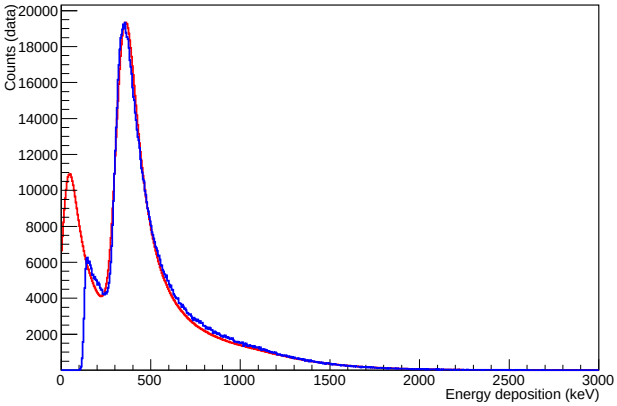

Figure 13: Energy deposition simulation. Blue represents data. Red is Monte Carlo with smear parameter set to 30 keV.

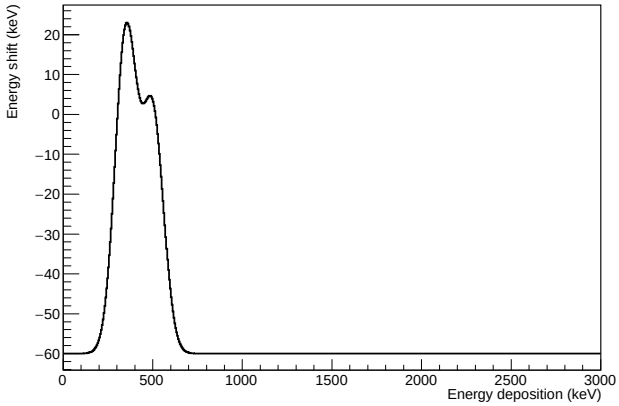

Figure 14: Potential energy shift versus energy deposition. The black line represents how much the data might be different than Monte Carlo.

applied to the simulation (described in section 4.1) were placed in a histogram with out-of-time hits subtracted.

Due to limited statistics, when the incident photon energy was less than 8.4 GeV or greater than 9.4 GeV, the tagger information was neglected. Effectively we are only extracting the tagged-flux within the energy range from 8.4 to 9.4 GeV. The events coming from the red region seen in Fig. 10 represented the TPOL out-of-time hits, and these were subtracted from those events with TPOL in-time events coming from the blue region.

When the incident photon energy was within the range 8.4 to 9.4 GeV, a two-stage out-of-time subtraction was performed. In the first stage, each TPOL event coming from either blue (TPOL in-time) or red (TPOL out-of-time) region from Fig. 10, had tagger out-of-time hits subtracted, where the tagger in-time hits are defined as having tagger time relative to PS within $\pm$ 2 ns (see Fig. 11) and tagger out-of-time hits are defined as being between -14 and -6 ns (two beam buckets). The tagger out-of-time hits were weighted by a factor of 1/2 to account for the fact that two beam buckets were used for the tagger out-of-time subtraction. The second stage of the subtraction was to simply subtract the TPOL out-of-time hits from the TPOL in-time events.

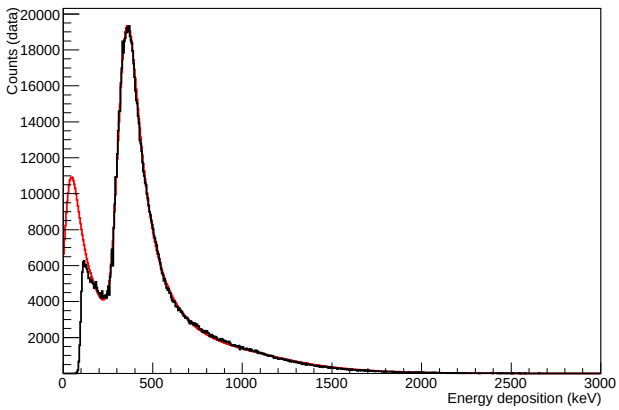

Figure 15: Comparison of Energy deposition simulation to data when data has been shifted. Blue represents data that has been shifted in energy by an amount shown in Fig. 14 . Red is Monte Carlo with smear parameter set to 30 keV.

The photon beam polarization for a particular run is defined as being either PARA or PERP in orientation. The PARA orientation had the photon beam polarization orientation parallel to the laboratory floor, while the PERP orientation had the photon beam polarization plane perpendicular to the floor. An example of an out-of-time subtracted yield distribution for PARA with incident photon energies from 8.4

to 9.0 GeV is provided in Fig. 16, where the solid line is a fit to the data using the function $A[1 + B\cos(2\phi - 2\phi_0)]\epsilon(\phi)$. The acceptance function $\epsilon(\phi)$ is due to the beam offset described in section 4.3, and has the form $[1 + F_0\cos(\phi - \phi_1)]$. For the example shown in Fig. 16, $F_0 = 0.011(1)$, which roughly corresponds to a beam offset of 0.1 mm. For the case of PERP, the first moment was found to be even closer to zero ($F_0 = 0.005(2)$). Fits were performed for the azimuthal yield distributions in 100-MeV-wide bins for energies from 8.4 to 9.0 GeV; these fits can be seen in Appendix A.

The determination of the degree of photon beam polarization was found by taking the value of B and dividing that value by the corresponding value of the beam asymmetry Σ obtained from the simulation (described in section 4.1). A plot showing the polarization for PARA and PERP orientations can be found in Fig. 17, where the blue points are for PARA while the red points are for the PERP orientation.

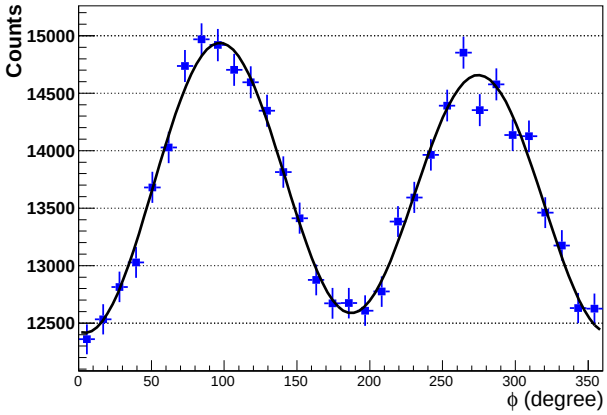

Figure 16: Counts versus azimuthal angle for PARA TPOL events with incident photon energies from 8.4 to 9.0 GeV.

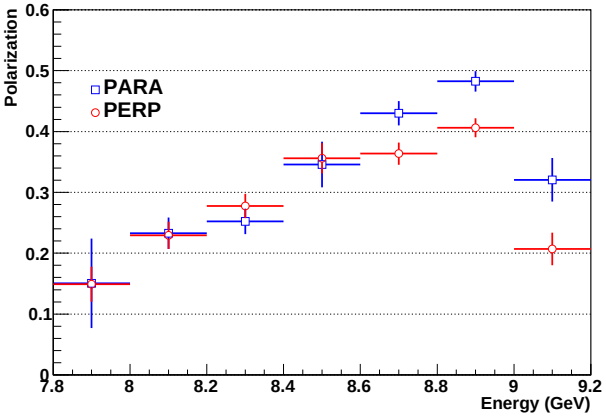

Figure 17: Polarization versus E_γ. Blue points represent PARA and red represents PERP.

6 Systematic and total uncertainty

The analyzing power of the TPOL detector is dependent upon having the simulation faithfully representing the TPOL device. If the simulation was a perfect representation of the TPOL, and assuming that the event generator worked correctly, then the polarization derived by use of the analyzing power would be correct. For this reason, uncertainties in the analyzing power used in the determination of the beam polarization are the main source of systematic uncertainty in the beam polarization measurement.

6.1 Sources of systematic uncertainty in the TPOL analyzing power

The interaction of photons from the incident photon beam with the converter causes recoil electrons and produced $\delta-$rays to strike the silicon strip detector. The number of $\delta-$rays and the amount of rescattering that occurs within the converter material both depend upon the thickness of the converter, which directly impacts the value of analyzing power.

For all particles that interact with the SSD, an energy threshold is required for that interaction to be classified as a detector hit. Thus, the energy calibration and resolution of the device also will

affect the accuracy of the analyzing power. Moreover, the sector-by-sector energy calibration can also affect the analyzing power accuracy.

The distance from the converter foil to the TPOL detector determines the minimum and maximum polar angle that the recoil and $\delta-$rays make with the detector and any uncertainty in the distance from foil to TPOL detector will impact the value of analyzing power.

As described previously (subsection 4.3) the beam offset can effect the analyzing power.

Since we cannot generate an infinite number of simulated events, there is a statistical limitation as to how well the analyzing power can be determined from the number of simulated events processed during the simulation.

In summary, then, the systematic contributions to the uncertainty in the photon beam polarization by the TPOL analyzing power determination are:

1. converter thickness,
2. distance from foil to TPOL,
3. energy cut,
4. sector-by-sector energy calibration
5. energy resolution,
6. beam offset,
7. analyzing power statistics.

6.2 Converter thickness uncertainty contribution

The manufacturer of the beryllium converter gives a tolerance of 0.0005 inch (12.7 μm) for the thickness of the material. Assuming that this tolerance represents three standard deviations, then the standard deviation would be 4.2 μm. The analyzing power has been determined for a converter thickness of 72.0, 76.2 (nominal) and 80.4 μm. We found that the largest percent difference in analyzing power from the case of using the nominal converter thickness was for the 80.4 μm converter thickness. The value obtained for the estimated systematic uncertainty associated with the converter thickness is $\sigma_\Sigma/\Sigma = 0.53\%$, where we are using Σ to represent the analyzing power.

6.3 Distance from foil to the SSD

The SSD is very sensitive and can not be touched by the survey equipment. A survey was performed to determine the distance from the center of the foil to the downstream face of the PCB that holds the SSD and was found to be 34.9 mm. Since the PCB is 2.4 mm thick, the distance from the foil to the center of the PCB is 33.7 mm, and that is the distance we use between the SSD and foil in the simulation. However, the SSD is 1 mm thick and we do not know the exact placement in the beam direction within the PCB. This means that we only know the placement of the SSD in the direction of the beam within 0.7 mm. When we simulate the analyzing power for an SSD that has been displaced +0.7 mm and -0.7 mm from the nominal position in the direction of the incident photon beam, we find that the maximum percent error (as compared to the nominal placement) is 0.54

6.4 SSD energy threshold cut uncertainty contribution

The energy cut used in the analysis of data and simulation results was 230 keV. As was seen in Fig. 14 from the previous section, the knowledge of the energy deposition could be off by as much as 80 keV. The analyzing power derived using a cut at 190 keV is 99.1% of the value had the cut been placed at 270 keV (difference of 80 keV in cut energy). Therefore, we take as an estimate of the systematic uncertainty of the analyzing power due to the energy cut to be $\sigma_\Sigma/\Sigma = 0.9\%$.

As discussed in the previous section, the energy resolution appears to have a standard deviation of about 30 keV. We do not know the exact value but we can be reasonably sure that the value must be between 10 and 50 keV (see Fig. 12). The analyzing power using a 10 keV smear is 0.5% larger than the case of a 50 keV smear. Thus, we take as a conservative estimate for the systematic uncertainty of analyzing power due to the energy resolution to be $\sigma_\Sigma/\Sigma = 0.5\%$.

6.5 Sector-by-sector calibration uncertainty contribution

The sector-by-sector energy calibration was found to be consistent within a standard deviation of 3 keV. We simulated 12 trials where the energy cut for a sector came from a random normal distribution of standard deviation equal to 3 keV. Using this procedure, we found that the uncertainty in the analyzing power due to the sector-by-sector calibration is 0.1%.

6.6 Beam offset uncertainty contribution

As discussed in sec 4.3 the systematic uncertainty associated with the beam offset is 0.71%.

6.7 Simulation statistical uncertainty contribution

The uncertainty in analyzing power due to simulation statistics over the range 8.4 to 9.0 GeV (the energy range used in the physics paper) is $\sigma_\Sigma/\Sigma = 0.2\%$, and we take that value as the systematic uncertainty in the simulation statistics.

6.8 Estimated uncertainty in TPOL beam polarization measurement

The estimated systematic uncertainty in the TPOL determination of polarization from each contribution discussed in this section is summarized in Table 1. Once each contribution is summed in quadrature, the total systematic uncertainty estimate is 1.5%.

Table 1: Estimated systematic uncertainty in the TPOL determination of polarization.

Source	Estimated systematic uncertainty (σ_Σ/Σ)
Converter thickness	0.53%
Converter distance	0.54%
Energy cut	0.9%
Sector-by-sector energy calibration	0.1%
Energy resolution	0.5%
Beam offset	0.71%
Analyzing power statistics	0.2%

7 Acknowledgments

Work at Arizona State University was supported by the National Science Foundation award PHY-1306737.

References

[1] L.C. Maximon, H.A. Gimm, Phys. Rev. A bf 23, 172 (81).

[2] `http://physics.nist.gov/PhysRefData/Xcom/html/xcom1.html`

[3] `http://www.linear.com/solutions/ltspice`

[4] J.H. Hubbell, *et al.*, J. Phys. Chem. Ref. Data , Vol.4, No.3 (1975).

Appendices

A TPOL fits

Plots of counts versus azimuthal angle can be found in figures 18-29.

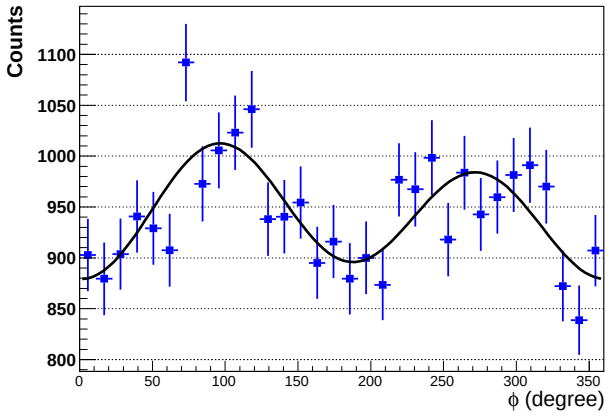

Figure 18: PARA setting at $E_\gamma = 8.45$ GeV.

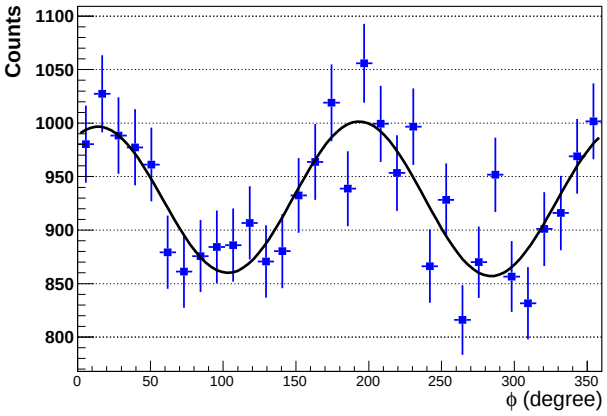

Figure 19: PERP setting at $E_\gamma = 8.45$ GeV.

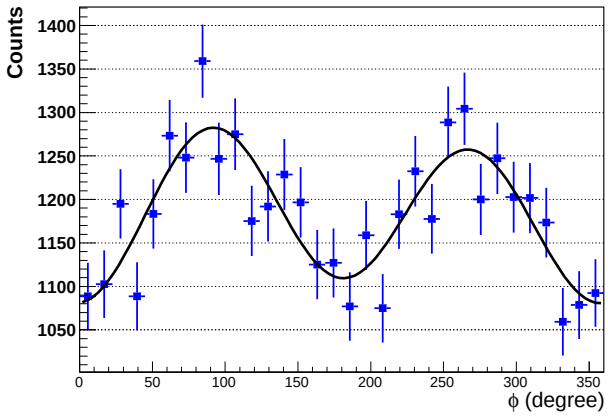

Figure 20: PARA setting at $E_\gamma = 8.55$ GeV.

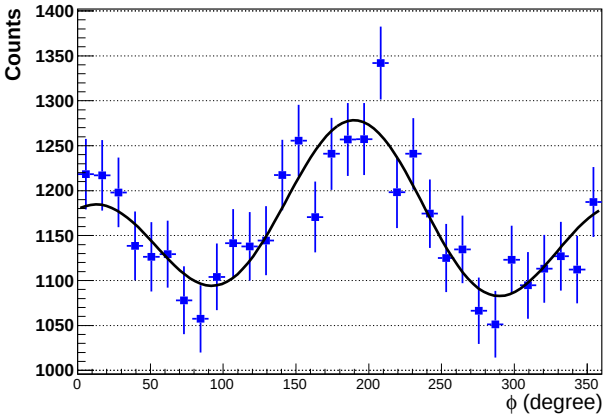

Figure 21: PERP setting at $E_\gamma = 8.55$ GeV.

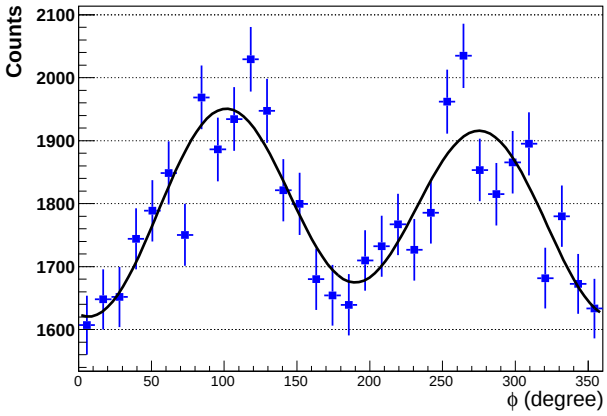

Figure 22: PARA setting at $E_\gamma = 8.65$ GeV.

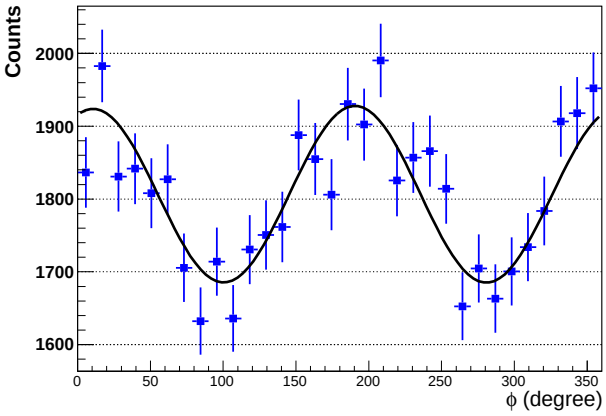

Figure 23: PERP setting at $E_\gamma = 8.65$ GeV.

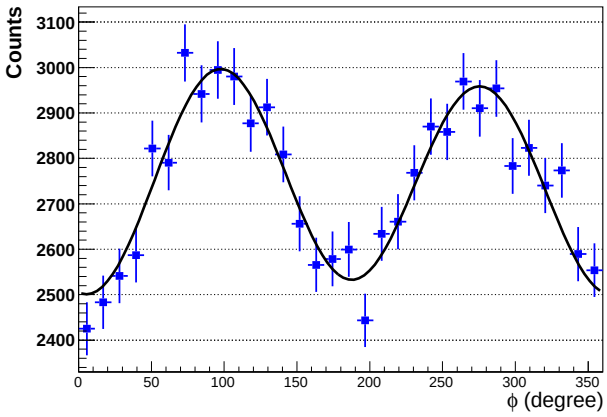

Figure 24: PARA setting at $E_\gamma = 8.75$ GeV.

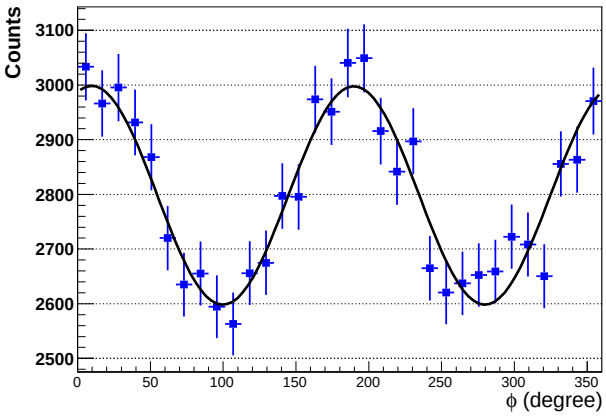

Figure 25: PERP setting at $E_\gamma = 8.75$ GeV.

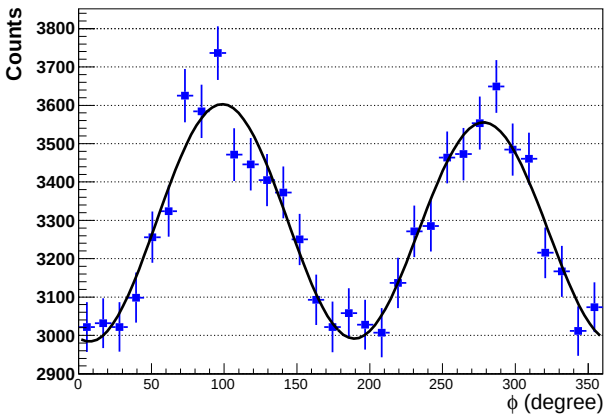

Figure 26: PARA setting at $E_\gamma = 8.85$ GeV.

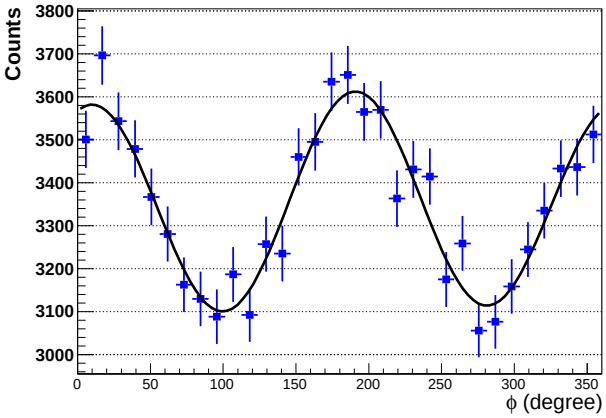

Figure 27: PERP setting at $E_\gamma = 8.85$ GeV.

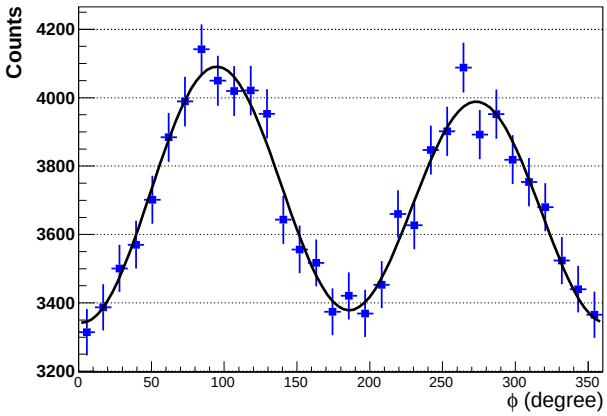

Figure 28: PARA setting at $E_\gamma = 8.95$ GeV.

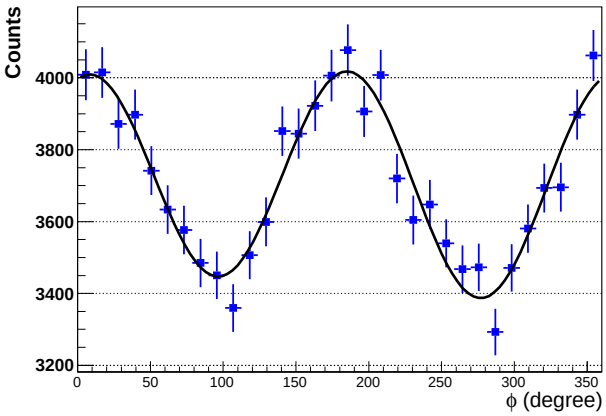

Figure 29: PERP setting at $E_\gamma = 8.95$ GeV.